

Experimental and theoretical coupled approaches for the analysis of radiative transfer in photoreactors containing particulate media: Case study of TiO2 powders for photocatalytic reactions

E. Ribeiro, G. Plantard, J.-F. Cornet, F. Gros, Cyril Caliot, V. Goetz

▶ **To cite this version:**

E. Ribeiro, G. Plantard, J.-F. Cornet, F. Gros, Cyril Caliot, et al.. Experimental and theoretical coupled approaches for the analysis of radiative transfer in photoreactors containing particulate media: Case study of TiO2 powders for photocatalytic reactions. Chemical Engineering Science, 2021, 243, pp.116733. 10.1016/j.ces.2021.116733 . hal-03280864

HAL Id: hal-03280864
https://cnrs.hal.science/hal-03280864

Submitted on 7 Jul 2021

HAL is a multi-disciplinary open access archive for the deposit and dissemination of scientific research documents, whether they are published or not. The documents may come from teaching and research institutions in France or abroad, or from public or private research centers.

L'archive ouverte pluridisciplinaire **HAL**, est destinée au dépôt et à la diffusion de documents scientifiques de niveau recherche, publiés ou non, émanant des établissements d'enseignement et de recherche français ou étrangers, des laboratoires publics ou privés.

Experimental and theoretical coupled approaches for the analysis of radiative transfer in photoreactors containing particulate media : case study of TiO_2 powders for photocatalytic reactions

E. Ribeiro[(*,1,2)], G. Plantard[(1,2)],J.-F. Cornet[(3)] , F. Gros[(3)] , C. Caliot[(4)] , and V. Goetz[(1)]

[(1)]PROMES CNRS, UPR 8521, Rambla de la thermodynamique 66100 Perpignan, France.
[(2)]University of Perpignan ViaDomitia, 52 Paul Alduy 66100 Perpignan, France.
[(3)]University of Clermont Auvergne, CNRS, SIGMA Clermont, Institut Pascal, F-63000 Clermont–Ferrand, France.
[(4)] Laboratory of Mathematics and its Applications, Université de Pau et des Pays de l'Adour, E2S UPPA, CNRS, LMAP, Allée du parc Montaury, 64600, Anglet, France.

* Corresponding author. Tel.: +33602311658; E-mail address: enrique.ribeiro@promes.cnrs.fr

Abstract

The analysis of radiative transfer in photoreactors is often crucial for operating efficient photoreactions. This article aims to present a complete experimental and theoretical coupled approach allowing radiative transfer analysis of photoreactors containing particulate media. TiO_2 powder, widely used in photocatalysis, was selected as a case study material for this work. First, Mie theory was used and adapted to assess the effective properties of heterogenous powders. A home-made experimental bench allowing normal-hemispheric transmittance measurement was settled. Theoretical and experimental evaluations of the radiative properties were compared and appear to match each other. The second part of the work consisted in both transmittance and local radiant energy modeling through Monte Carlo and Two Flux models using the previously defined radiative properties as entry parameters. The comparison of experimental and modeled transmittance highlighted the consistence of these models which were then used to describe the radiant energy evolution inside a parallel-plane photoreactor.

Keywords: Photoreactor; radiative transfer; Experimental bench; modeling; Monte Carlo; TiO_2

1. Introduction

Photoreactors and their design raised as an important field of interest in both photobiology and photochemistry processes. The attractivity of this topic comes from interesting new applications for which photoreactors are efficient. For instance, photobioreactors were efficiently developed for microalgae growth in the field of biofuels productions [1-3]. Alongside photochemistry, water treatment by photocatalysis was widely investigated, leading to an abundant literature on designing photoreactors for such processes [4,5,6]. The specificity of photo(bio)reactors in relation to conventional reactors neither lies about their ability to mix the compounds nor on mass transfer, but on the use of light and its ability called actinism, to generate reactions with biochemical and chemical systems [7]. This capacity assessment depends on many parameters: light source and reactor geometries, reactor contents… The description of photocatalytic reactions indeed requires to establish relations for mean rates from these parameters and the radiant energy flux Φ_0 incident onto the reactor. In the most simple cases, the mean volumetric reaction rate $< r >$ is linearly dependent on the mean local volumetric rate of radiant energy absorbed <*A*> (MVREA) which may be obtained by different simple methods without a comprehensive description of radiative transfer inside the reactor. For example, two different assessment methods are well established: (i) the use of photonic phase balance from experimental measurement of Φ_0 and transmittances [8]; (ii) the $< A >$ assessment by ensuring that all incident photons are absorbed inside the reactor [9,10].

However, a lot of photoreactions and photobioreactions were shown to be non-linearly dependent on the incident radiant energy [11,12,13]. In such cases, the radiative transfer equation resolution is necessary to access the local quantity of absorbed photons within the medium. The widely investigated heterogeneous photocatalysis using TiO_2 catalyst is a good case study of reaction for which this difficulty is ubiquitous. It can be briefly reminded that this process consists in the generation of radical molecules, *i.e.* $OH^{\bullet}$ and $O_2^{-\bullet}$, from water and dissolved oxygen by simple redox mechanisms involving charges generated

from the photo-excitation of the catalyst [14,15]. From an application perspective, the degradation kinetics of many organic compounds induced by photocatalysis was investigated and often revealed a non-linear dependence of the kinetic relative to the incident radiant energy [16,17,18], making it necessary to assess the local available radiant energy by radiative transfer study. Many authors have made strategic choices such as supporting the catalyst on a surface which allows to avoid the need of studying the radiant energy extinction through the photoreactor volume [6,19,20]. However, it was shown that this choice simplified the radiative study at the expense of the catalyst performance, compared to other forms such as suspensions and foams supported catalysts [21]. Indeed, catalyst suspension is the form which exhibits the highest photocatalytic performances and is thus an attractive choice for efficient photocatalytic applications. To go further in the understanding in the use of suspensions, it then requires the assessment of the Local Volumetric Rate of radiant light Energy Absorbed (LVREA) which is only possible by radiative transfer analysis if the medium (solvent + particles) optical properties are well defined.

The aim of this work is to present a theoretical and experimental approach for measuring and validating the radiative properties of suspended particles, and then to model the local radiant energy in a system containing these materials. The study relies on a TiO_2 catalyst as a case study and could be extended to other particulate systems, the method being generic. The first section will be dedicated to the theoretical study of the radiative properties of the particles and their validation by experimental measurement on an optical bench. The second part will be devoted to the comparison between experimental measurements of a cell (assimilated to a parallel-plane reactor) and theoretical results based on two radiative transfer models: one based on an analytical two-flux approximation and the other based on the rigorous solution of the radiative transfer equation using the stochastic Monte Carlo method. An originality of this work is the theoretical transmittance assessment by considering cell

interface effects on both Monte Carlo and two-flux simulations, which has not been addressed before to the authors knowledge. Finally, the local radiant available energy and the LVREA within the system will be described through the two models and discussed.

2. Experimental

2.1. Suspension characteristics

Commercial VP Aeroperl ® P25/20 TiO_2 powder was selected and purchased from Evonik. The material is composed of 85% anatase and 15% rutile phases. Morphology and particle size are determinant characteristics from a radiative transfer perspective. Thus, the powder granulometry and morphology were characterized by Scanning Electron Microscopy (SEM) and normalized Dynamic Light Scattering (DLS) method, using respectively a SEM-FEG Hitachi S-4500and a Mastersizer 3000 devices.

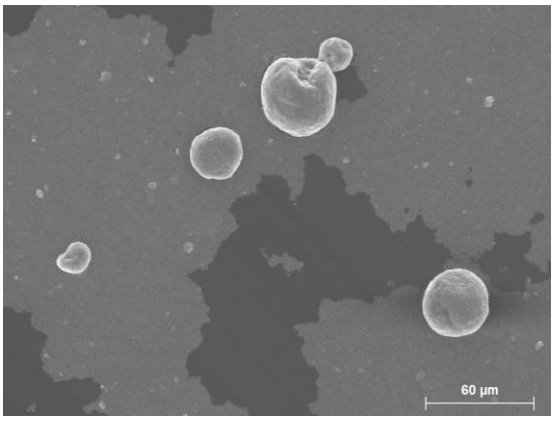


Figure 1. *Scanning Electron Images (SEM-FEG, Hitachi S-4500) of commercial Aeroperl® P25/20 TiO_2 particles. Magnification ×400.*

The TiO_2 powder image (Figure 1) was acquired with a secondary electron detector and a 15 kV electron beam, at a working distance of 14 mm. The TiO_2 powder is composed of spherical shaped micrometric particles. The granulometric analysis (Figure 2) of the powder highlights a log-normal particle size distribution and confirm the micron scale with a mean diameter of the powder particles of 41 µm and a standard deviation of 17 µm.

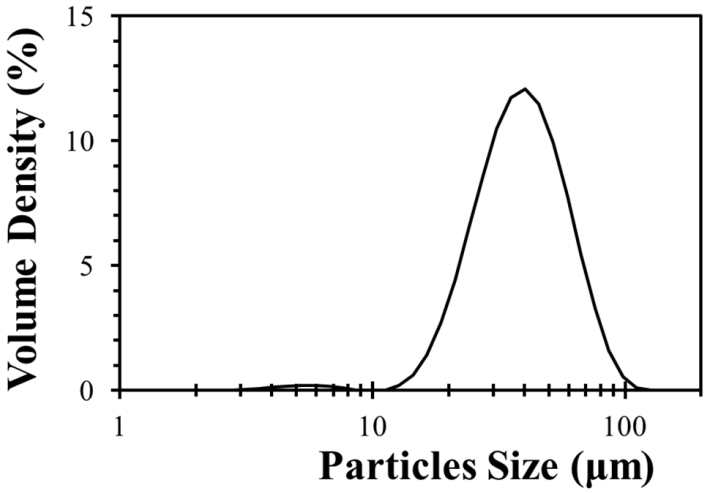


Figure 2. *Volumetric particle size distribution ofAeroperl® P25/20 powder provided by Dynamic Light Scattering (DLS).*

Another important characteristic to the study of optical properties is the complex refractive index $m_\lambda = n_\lambda - i\kappa_\lambda$ which is decomposed in a real part n_λ and an imaginary one κ_λ. The complex refractive index of TiO_2 have been thoroughly investigated, leading to abundant TiO_2 n_λ and κ_λ data which cover both a wide scale of wavelength from UV to infrared and different TiO_2 crystalline phases [22-26]. In the literature, these properties differ whether the material form is a thin layer or a powder [27,28]. Complex refractive index values handled in this work were thus extracted from the work of Jalava et al. [28] whose assessed the n_λ and κ_λ values of anatase and rutile for particles.

	Rutile		**Anatase**	
Wavelength (nm)	**n**	**κ**	**n**	**κ**
325	3.17	0.710	2.858	0.134
350	2.931	0.175	2.535	0.039
370	2.7678	0.118	2.4046	0.0078
375	2.727	0.104	2.372	0
400	2.589	0.018	2.278	0
500	2.429	0	2.270	0
800	2.331	0	2.103	0

Table 1. *Powder TiO_2 refractive index n and κ of Rutile and Anatase collected from [28] at different wavelengths from near UV to visible wavelength.*

The Aeroperl® P25/20 effective constants were then calculated from these values, reported in Table 1, using the well-known Bruggeman mixing formula [29,30] represented by the following equation (1):

$$f_i \frac{\hat{\varepsilon}_{r,i} - \bar{\hat{\varepsilon}}_{r,mix}}{\hat{\varepsilon}_{r,i} + 2\bar{\hat{\varepsilon}}_{r,mix}} + (1 - f_i) \frac{\hat{\varepsilon}_{r,h} - \bar{\hat{\varepsilon}}_{r,mix}}{\hat{\varepsilon}_{r,h} + 2\bar{\hat{\varepsilon}}_{r,mix}} = 0 \quad (1)$$

where $\bar{\hat{\varepsilon}}_{mix}$ is the effective complex permittivity of the mixed material, $\hat{\varepsilon}_i$ is the inclusion complex permittivity, $\hat{\varepsilon}_h$ the host medium complex permittivity and f_i the volume fraction of inclusion. Note that this equation is symmetrical, meaning that the mix effective permittivity would be identical whether anatase or rutile is chosen as the host medium. The obtention of the effective complex permittivity of the mixture from Bruggeman formula allowed the calculation of the complex refractive index of Aeroperl® P25/20 using the simple relation $m_\lambda = \sqrt{\hat{\varepsilon}_\lambda}$. The calculated spectral distribution of the real and imaginary part of the TiO_2 powder refractive index in the wavelength range of 350-500 nm is shown in Figure 3.

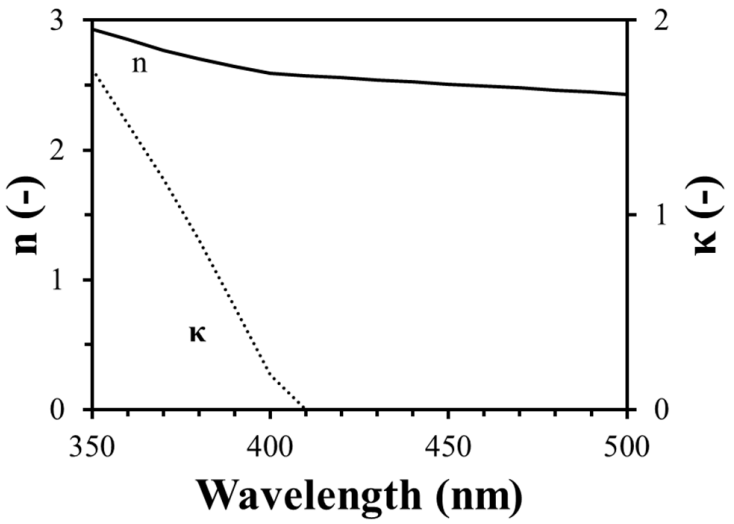


Figure 3. *Mean refractive indexes n and κ of 85/15 Anatase/Rutile TiO_2 mixture using Bruggeman mixing rule.*

For the need of the work, 250 mL TiO_2 suspensions were prepared by dispersing TiO_2 powder in deionized water (18 MΩ). In order to investigate the optical properties of TiO_2, ten suspensions with different TiO_2 concentrations were realized, i.e. 0.01; 0.02; 0.05; 0.1; 0.2; 0.3; 0.4; 0.5; 1.0 and 3.0 $kg.m^{-3}$.

2.2. Optical measurement setup and protocol

An optical bench was set up to characterize the optical response, i.e. the transmittance, obtained while irradiating the TiO_2 suspensions with a collimated light in the near UV to visible wavelength range.

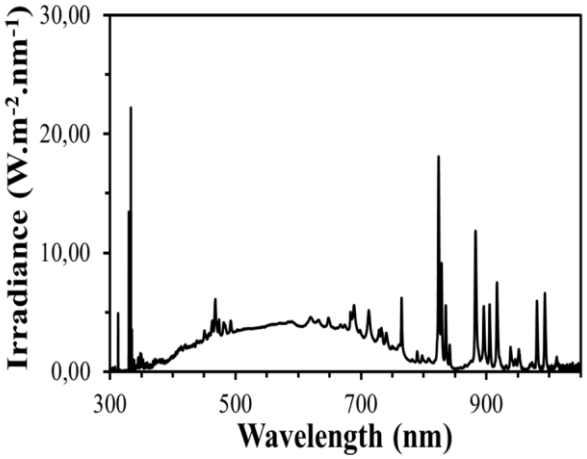


Figure 4. *Solar lamp irradiance spectrum from near UV to near infrared wavelength.*

To meet this objective, the testbench comprises a solar-like spectrum 1000W collimated source (Figure 4), a 2 cm thick measurement cell containing the tested suspension between Polymethyl methacrylate (PMMA) walls, and a spectrophotometer-coupled integrating sphere. As the bench scheme reported in Figure 5 illustrates, the collimated source is irradiating the whole measurement cell surface.

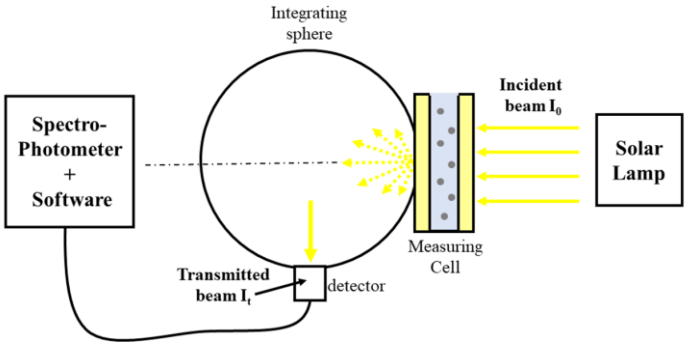


Figure 5. *Schematic of the optical bench set up for experimental assessment of the transmittance.*

The light crossing the 2 cm thickness cell has undergone multiple diffusion events. Thus, the role of the integrating sphere placed against the opposite side of the cell is to collect and integrate both direct and diffuse radiant contribution through the 7 cm² aperture of the sphere. The radiant energy exiting the suspension is measured by coupling the integrating

sphere to an Ocean Optics spectrophotometer (HR4000 High-Res; detection range: 250-1100 nm). The software acquisition settings were selected as follows: First, the wavelength detection was restricted to the range 350-500 nm to cover both active and inactive wavelength range of the TiO_2 catalyst. Secondly, the representativity and repeatability of the tests were ensured by doing three measurements for each suspension, covering an integration time of 5 sec. This acquisition time is composed of 25 analysis of 200 ms, each corresponding to the collection of 3×10^{14} photons in our conditions. The experimental measurement consisted in three steps: (i) The ambient radiant noise is registered to be removed from the measure, (ii) the incident flux $\Phi_{0,\exp}$ is measured and registered as the maximum transmitted reference signal, (iii) the suspension is inserted in the measuring cell which is then introduced between the lamp and the light-integrating sphere and a transmittance measurement is done. It can be remembered that the transmittance corresponds to amount of radiant energy which leaves a system. It can be absolute or relative. Here we measure the relative transmitted flux $\Phi_{t,\exp}$ normalized between 0 and 1 by reporting the obtained absolute transmittance value to the $\Phi_{0,\exp}$ reference. During the experiment, the TiO_2 particles dispersion in water is maintained using a magnetic-stirrer.

2.3. Radiative properties theoretical predictions

The calculation of radiative properties is possible thanks to the pioneer work of Lorenz-Mie who solved Maxwell equations for the problem of a plane wave diffraction by a spherical particle a long time ago [31,32]. Mathematical considerations around Mie solution which has a form of infinite series requiring to compute spherical Riccati-Bessel functions will not be reminded there, as it is already well reported elsewhere [33]. This theoretical approach was formalized through the well-known BHMIE program written by Bohren and

Huffman [33]. Their algorithm lead to the rigorous calculation of the intrinsic radiative properties of a single spherical particle experiencing independent scattering, i.e. the extinction, scattering, absorption and backscattering efficiencies respectively annoted Q_{ext}, Q_{sca}, Q_{abs} and Q_{back}, and the angle-dependent scattering function $p_\lambda(\vec{\Omega},\vec{\Omega}')$. Absorption, scattering, and extinction coefficients, respectively k_{abs}, k_{sca} and k_{ext} (m^{-1}) can be derived from these efficiencies (see hereafter) and are of better interest to characterize the optical behavior of a medium [34]. The program requires only three entry parameters, which are the particle diameter D, the material density ρ and its complex refractive index for a given wavelength λ. It was shown that Mie theory can be consistently used meeting this condition: The studied particle is spherical/quasi-spherical shaped. Note that when the size parameter $x = \pi D n_{medium,\lambda} / \lambda$ value is low ($x << 1$), the Rayleigh approximation can also be used [35,36]. At the opposite, if the size parameter is very high ($x >> 1$), the geometrical optics approximation can be used instead of Mie solution [33].

The two above described constraints are met in this work. Indeed, SEM image (Figure 1) observation led us to assert that the Aeroperl® P25/20 TiO_2 powder is composed of spherical particles. Also, the particle size distribution analysis (Figure 2) showed that the TiO_2 particle diameters were in the range 3-115 µm, corresponding to a size parameter x in the range 25-1000 for our irradiating conditions, from near UV to visible wavelength (350-500 nm). Thus, the BHMIE program was adapted and used to obtain both the effective absorption/scattering coefficients and phase function of the studied TiO_2 considering the size distribution by simply integrating the radiative properties over the total number of particles (per unit volume) defined by:

$$N_T = \frac{f_v}{V_P} = \int_0^\infty n(D)dD \qquad (2)$$

Where N_T is total number of particles per unit volume (m^{-3}), f_v is volume ratio of particles in the water medium (m^3/m^3), V_P is particles volume (m^3) and $n(D)$ is the volumetric particle size distribution function. The obtention of the effective absorption/scattering/extinction coefficients and phase function of the powder was reached by the following integrations (Eq. (3) and (4)):

$$k_{abs/sca/ext,\lambda} = \frac{\pi}{4}\int_0^\infty D^2 Q_{abs/sca/ext,\lambda} n(D) dD \tag{3}$$

$$p_\lambda(\vec{\Omega},\vec{\Omega}') = \frac{\int_0^\infty D^2 Q_{sca,\lambda}\, p(D,\vec{\Omega},\vec{\Omega}') n(D) dD}{\int_0^\infty D^2 Q_{sca,\lambda} n(D) dD} \tag{4}$$

Where $k_{abs/sca/ext,\lambda}$ are the effective absorption, scattering, and extinction coefficients (m^{-1}). These coefficients are dependent on the suspension concentration. Thus, the effective specific absorption, scattering, and extinction coefficients $E_{abs,\lambda}, E_{sca,\lambda}, E_{ext,\lambda}$ defined in the Eq. (5) below will be preferred in this work. Indeed, these values are constant from one concentration to another and thus characterize an intrinsic property of TiO_2 powder:

$$E_{abs/sca/ext,\lambda} = \frac{k_{abs/sca/ext,\lambda}}{C_{susp}} \tag{5}$$

Where $E_{abs/sca/ext,\lambda}$ are the specific absorption/scattering/extinction coefficient ($m^2.kg^{-1}$), and C_{susp} is the suspension concentration ($kg.m^{-3}$).

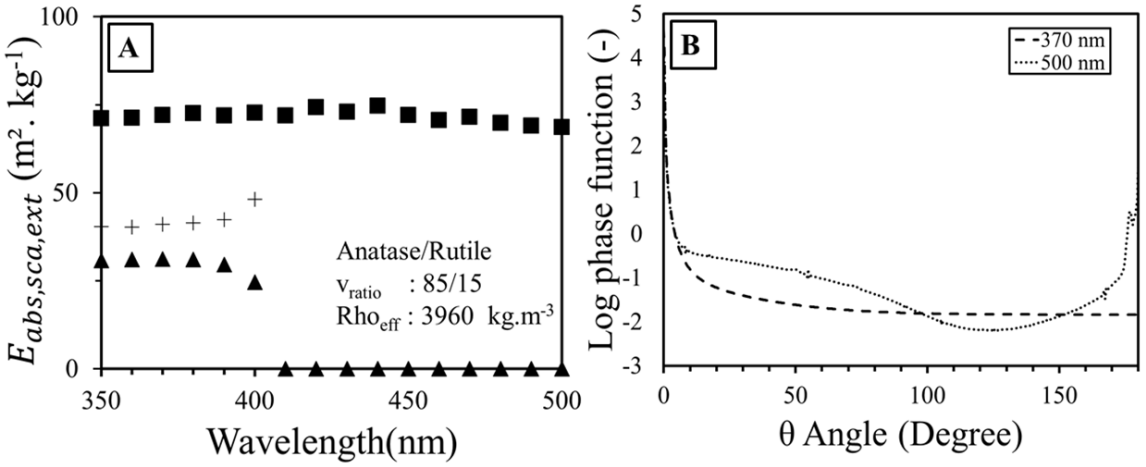


Figure 6. *TiO_2 radiative properties assessed by Mie theory: absorption (▲), scattering (+) and extinction (■) specific coefficients from near UV to visible wavelength (A); angle-dependent scattering function in near UV and visible spectral region (B).*

The theoretical specific coefficients extracted from BHMIE and reported on Figure 6.A show that TiO_2 optical behavior is composed of an absorption and scattering part in UV region. This observation is in good agreement with the semiconductor behavior of TiO_2. Indeed, the material band-gap activation energy around 3.0 eV for rutile phase suggests that the photo-excitation phenomenon occurs only for photons whom wavelengths are lower than 413 nm. Thus, photons meeting this condition can be absorbed by the material. This phenomenon is well traduced there, as the specific absorption coefficient $E_{abs,\lambda}$ is null in the visible region and increases in the near UV region to a value as high as 35 $m^2.kg^{-1}$ at 360 nm. On the other hand, the scattering effect is high and constant in the visible region, where the specific scattering coefficient value is around 80 $m^2.kg^{-1}$, and decreases in the UV region to a value as low as 45 $m^2.kg^{-1}$ at 360 nm. Note that the specific scattering and absorption coefficients evolve symmetrically and two observations are interesting regarding the specific extinction coefficient $E_{ext,\lambda} = E_{abs,\lambda} + E_{sca,\lambda}$ and: (i) The extinction effect of TiO_2 is roughly constant along the whole interest wavelength scale and (ii) for the visible wavelength

range, $E_{ext,\lambda} = E_{sca,\lambda}$ which correspond to the well-known conservative case of the radiative heat transport theory [37].

The phase function $p_\lambda(\vec{\Omega},\vec{\Omega}')$ is dependent on the direction $\vec{\Omega}$ defined by the solid angle Ω which is composed by the polar angle θ and the azimuthal angle ϕ (Eq. (6)):

$$\frac{1}{4\pi}\iint_{4\pi} p_\lambda(\vec{\Omega},\vec{\Omega}')d\Omega = \frac{1}{4\pi}\int_0^{2\pi}\int_0^{\pi} p_\lambda(\theta,\phi,\theta',\phi')\sin\theta d\theta d\phi = 1 \quad (6)$$

It should be reminded there that for spherical particles, the angle-dependent scattering function $p_\lambda(\vec{\Omega},\vec{\Omega}')$ presents a symmetry and its definition no longer explicitly depends on the azimuthal angle ϕ (Eq.(7)):

$$\frac{1}{4\pi}\int_0^{2\pi}\int_0^{\pi} p_\lambda(\theta,\phi,\theta',\phi')\sin\theta d\theta d\phi = \frac{1}{2}\int_0^{\pi} p_\lambda(\theta,\theta')\sin\theta d\theta \quad (7)$$

The angle-dependent scattering function $p_\lambda(\theta,\theta')$ was reported for 1000 discrete θ angle values between 0 and π on Figure 6.B for two wavelengths: (i) 360 nm to represent phase function in the non-conservative case which correspond to near UV region where the semiconductor is absorbing light and (ii) 500 nm to observe the angular dependence of the phase function in the conservative case corresponding to the visible wavelength region. First, we asserted from Figure 6.B. that light is strongly scattered forward by TiO_2 particles in both cases. The base-10 logarithmic representation of each angle contribution allowed to highlight that there is a four order of magnitude difference between the proportion of light scattered straight forward and the proportion of light scattered in other directions for the UV wavelength region. In the visible wavelength range, the TiO_2 angle-dependent scattering function is less directional. $p_{500\,nm}(\theta,\theta')$ is characterized by a three order of magnitude

difference between the light scattered straight forward and through other directions. At the 360 and 500 nm wavelength, the asymmetry parameter $g = \frac{1}{4\pi}\iint_{4\pi} p\cos\theta d\Omega$, that characterizes the way a particle scatters incident light, was found to be 0.88 and 0.77 respectively. Reminding that the maximum asymmetry parameter value (g> = 1) corresponds an exclusively forward-oriented scattering, the <g> values found at 360 and 500 nm for TiO_2 confirm the strong forward-orientation of the phase function for these two wavelengths.

2.4. Experimental results and theoretical calculation comparison

The observations provided through theoretical calculations led us to assume that in our experimental conditions and in the UV wavelength region, for sufficiently diluted TiO_2 suspension, the specific absorption coefficient of TiO_2, $E_{abs,\lambda}$, can be assessed using the Beer-Lambert law (Eq. (8)):

$$T_\lambda = \frac{\Phi_{t,\lambda}}{\Phi_{0,\lambda}} = e^{-E_{abs,\lambda} C_{susp} L} \tag{8}$$

This approach is only consistent if in-scattering can be ignored and light extinction phenomenon along the suspension optical path is only due to absorption. Respecting these conditions, it is then possible to identify $E_{abs,\lambda}$ from a normal-hemispherical transmittance measurement (T_NH) [38]. Thus, this assessment was possible in our work as: (i) the contribution of absorption represents almost the half of the extinction phenomenon in the UV region, and (ii) in-scattering is strongly straight-forward-directed.

Our experimental approach consisted in TiO_2 transmittance measurements from concentrated to diluted suspensions to identify the specific absorption coefficient $E_{abs,\lambda}$ in the UV region and to compare it to theoretical predictions. Spectral transmittance

measurements reported in Figure 7.A show the evolution of the light fraction transmitted through the cell as the suspension concentration increases. The different optical behaviors of TiO_2 in UV (350-390 nm) and visible (390-500 nm) spectral ranges, described in section 2.3., are noticeable. The higher the suspension concentrations, the higher the gap between transmitted light in UV and visible ranges. In UV, the transmittance falls to a measured value as low as 0.1 for the more concentrated TiO_2 suspension, i.e. 3.0 $kg.m^{-3}$, and tends to values close to 1 for the more diluted suspensions, i.e. 0.02 and 0.01 $kg.m^{-3}$.

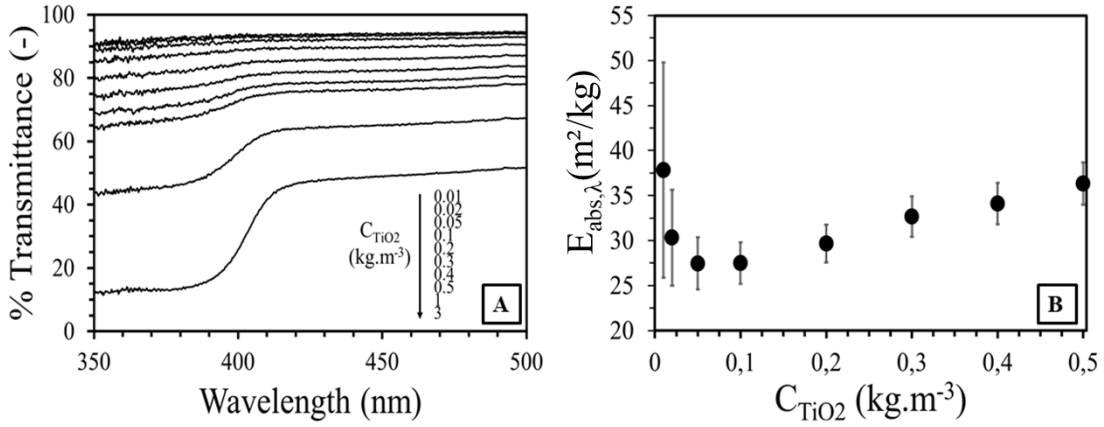


Figure 7. *TiO_2 suspension, experimental transmittance measurement of different concentrations, from near UV to visible wavelength (A). Mean $E_{abs,360\text{-}390\ nm}$ was calculated from experimental transmittance and represented as a function of concentration (B).*

The specific absorption coefficient $E_{abs,\lambda}$ is expected to be assessed at low concentration, such as the scattering event numbers tends to single scattering conditions [39]. The mean specific absorption coefficient $\overline{E}_{abs,360-390}$ calculated in the range 360-390 nm from transmittance experiments using the equation (8) and reported on Figure 7.B is subject to a variation with TiO_2 suspension concentration. Indeed, a lowering in concentration from 0.5 to 0.05 $kg.m^{-3}$ induced a decrease on the specific absorption coefficient estimated value from 36 to 27.5 $m^2.kg^{-1}$. This observation is consistent with a diminishing number of scattering events with the decrease of the suspension concentration. However, for concentration below

0.5 kg.m^{-3} an increase of the specific absorption coefficient is obtained to a value as high as 37.8 m².kg^{-1} for the lowest suspension concentration, i.e. 0.01 kg.m^{-3}. The higher error bar observed for the lowest concentrated suspension clearly indicates that we failed to reliably identify the specific absorption coefficient for very diluted concentrations.

Regarding $E_{abs,\lambda}$, the gap between the experimentally defined value, i.e. 28 ± 5 m².kg^{-1}, and the mean theoretical value calculated in the range 360-390 nm, i.e. 31.75 m².kg^{-1}, is lower than 5%. The difference between experimental approach and theoretical predictions is thus satisfactory. The excellent agreement of $E_{abs,\lambda}$ determined by Mie and the one defined by experimental inversion is a remarkable result which reconciles electromagnetism with radiative transfer throughout the settled optical bench. The developed optical bench, composed by a collimated source irradiating the entire surface of a measuring cell and an integrating sphere to collect the out-going light right against the opposite side of the cell, behave like a conventional optical bench for simple scattering inversion experiments.

3. Radiative Transfer Equation solutions applied to measuring cell

The literature on the resolution of the radiative transfer equation is rich, and many different methods were investigated in order to describe the local radiant energy and quantify the total energy absorbed or transmitted in system such as photo-reactors and photo-bioreactors. Among these methods, the stochastic Monte-Carlo method is a reference method that accounts for directional and spectral radiative properties in complex geometry without increasing the computation time [40]. Moreover, different approximate methods were investigated. For example, considering photoreactors or photobioreactors modeling, the single-scattering, the P_1 and the Two-Flux approximations were discussed and compared in [41]. To validate the effective radiative properties of the TiO_2 suspension we investigated to model the transmitted radiation by two different approaches: (i) a rigorous Monte-Carlo (MC)

method used as a reference and (ii) a Two-Flux (TF) analytical approximation in the considered one-dimensional Cartesian geometry.

3.1. Monte-Carlo method

The Radiative Transfer Equation (RTE), Eq. 9, is used to model the transport of radiation throughout the media. The effective radiative properties of the TiO_2 particle polydispersion in water defined in above sections (phase function, absorption and scattering coefficients) are assumed as known parameters in the equation:

$$\vec{\Omega}.\vec{\nabla} I_\lambda(\vec{u},\vec{\Omega}) = -(k_{abs,\lambda} + k_{sca,\lambda}) I_\lambda(\vec{u},\vec{\Omega}) + \frac{k_{sca,\lambda}}{4\pi} \iint_{4\pi} p_\lambda(\vec{\Omega},\vec{\Omega}') I_\lambda(\vec{u},\vec{\Omega}') d\Omega' \tag{9}$$

where $I_\lambda(\vec{u},\vec{\Omega})$ represents the radiative intensity ($W.m^{-2}.sr^{-1}$). Conditions at the interfaces are needed to consider the refractive index difference between the PMMA plate and the TiO2 suspension in water. Assuming smooth interfaces where specular reflection and refraction occur with the reflectivity (noted as $\rho_{\lambda,i\to t}$) given by Fresnel's relations, the transmitted radiative intensity I_t depends on the incident radiative intensity I_i and is given by:

$$n_{t,\lambda}^2 . I_{i,\lambda}(\vec{u},\vec{\Omega}_i)(1-\rho_{\lambda,i\to t}(\vec{u},\vec{\Omega}_i)) = n_{i,\lambda}^2 I_{t,\lambda}(\vec{u},\vec{\Omega}_t) \tag{10}$$

Fig. 8 depicts the one-dimensional geometry of the radiation problem, setting the observation direction $\vec{u}$ and the cell surfaces normal $\vec{n}$ colinear to the x axis.

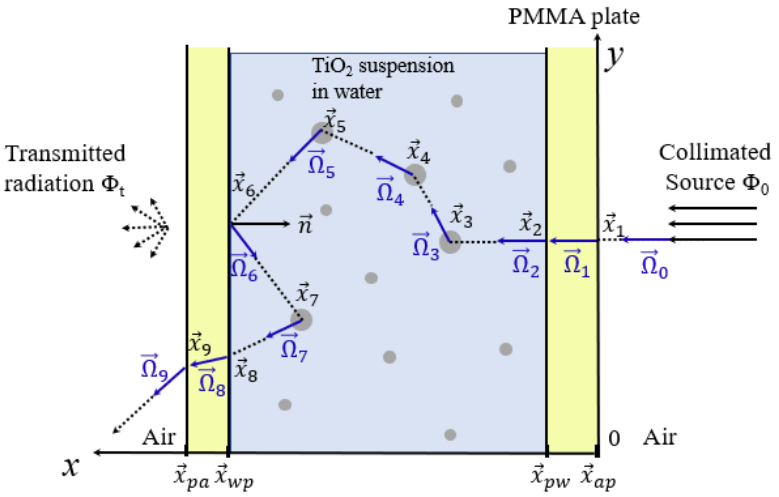


Figure 8. *Schematic of the transmitted radiation through a TiO2 suspension in water enclosed between PMMA plates. One possible path is drawn: The bundle of rays is displayed from the collimated source direction, it crosses the two PMMA interfaces (with air,* $\vec{x}_1$ *, and water* $\vec{x}_2$*) and experiences scattering events (*$\vec{x}_3 \rightarrow \vec{x}_5$*) until reaching a PMMA interface where reflection can occur (such as at* $\vec{x}_6$*, with local normal* $\vec{n}$*), or refraction (such as at* $\vec{x}_8$ *) which can lead to transmission in air or TIR inside the PMMA plate (at* $\vec{x}_9$*).*

The radiative flux from the source $\Phi_{0,\lambda}$ is assumed collimated($I_\lambda(\vec{x}_0,\vec{\Omega}) = \delta(\vec{\Omega}-\vec{\Omega}_0)I_{0,\lambda}$) and the radiative flux from the source is thus:

$$\Phi_{0,\lambda}(\vec{x}_0) = \int_{2\pi} I_\lambda(\vec{x}_0,\vec{\Omega})\left|\vec{n}(\vec{x}_0).\vec{\Omega}\right| d\Omega = I_{0,\lambda}\cos(\theta_0) \qquad (11)$$

Moreover, since the incident direction is normal to the PMMA plate, $\cos(\theta_0)=1$, and assuming $I_{0,\lambda}$ is unity, $\Phi_{0,\lambda}=1\text{W.m}^{-2}$. Then, the transmittivity is directly obtained from the computation of the transmitted flux, as $\Phi_{t,\lambda}=T_\lambda\Phi_{0,\lambda}$. The MC estimation of the transmitted flux was achieved representing the source radiative flux by bundles of rays which are followed until they are transmitted, reflected (back to the source side, or by Total Internal Reflection, TIR, in the PMMA), or absorbed by the colloidal medium.

A solution of the RTE (Eq.9) with the above described boundary conditions is the monochromatic radiant intensity $I_\lambda(\vec{x},\vec{\Omega})$ incident on the detector, defined by the integral formal solution (Eq.12):

$$I_\lambda(\vec{x},\vec{\Omega}) = I_\lambda(\vec{x}_{it},\vec{\Omega})e^{-\int_0^l k_{ext,\lambda}(\vec{x}-\tau\vec{\Omega})d\tau}$$

$$+\int_0^l d\tau e^{-\int_0^\tau k_{ext,\lambda}(\vec{x}-\tau'\vec{\Omega})d\tau'} \times \frac{k_{sca,\lambda}(\vec{x}')}{4\pi} \int_{4\pi} p_\lambda(\vec{\Omega},\vec{\Omega}')I_\lambda(\vec{x}',\vec{\Omega})d\Omega' \quad (12)$$

$$I_\lambda(\vec{x}_{it},\vec{\Omega}_r) = I_\lambda(\vec{x}_{it},\vec{\Omega}_i)\rho_{i\to t}(\vec{x}_{it},\vec{\Omega}_i) \quad (13)$$

$$I_\lambda(\vec{x}_{it},\vec{\Omega}_t) = I_\lambda(\vec{x}_{it},\vec{\Omega}_i)(1-\rho_{i\to t}(\vec{x}_{it},\vec{\Omega}_i))\frac{n_{t,\lambda}^2}{n_{i,\lambda}^2} \quad (14)$$

With $\vec{x}' := \vec{x} - \tau\vec{\Omega}$, l is the distance from $\vec{x}$ to the colloidal medium boundary (water-PMMA interface) in the direction $-\vec{\Omega}$ and $\vec{x}_{it} := \vec{x} - l\vec{\Omega}$ is the source location (reflected and refracted radiation) at the interface. The first term in the right-hand-side of Eq.12 is the directly transmitted contribution from the source at the interface and the second term corresponds to the contribution of multiply scattered radiative intensity coming from the source. Eq. 13 and 14 give the reflected and refracted radiative intensity at an interface and ray directions follow the Snell's law.

The generalized path integral formulation introduced in the Veach's thesis [42] was followed and the application to participating media by Pauly et al. [43] was used to develop a forward Monte-Carlo algorithm, computing the transmitted flux with the relations:

$$\Phi_{t,\lambda}(\vec{x}) = \int_{2\pi} I_\lambda(\vec{x},\vec{\Omega})\left|\vec{n}.\vec{\Omega}\right| d\Omega(\vec{\Omega}) \approx \Phi_{t,\lambda,MC} \quad (15)$$

$$\Phi_{t,\lambda,MC} = \frac{1}{N}\sum_{i=1}^{N} W_i \tag{16}$$

$$I_\lambda(\vec{x},\vec{\Omega}) = \int_0^\infty \mathrm{P}_{L_{sca},\lambda} e^{-k_{abs,\lambda} l_{sca}(\vec{x}')} d\vec{x}' \frac{1}{4\pi} \int_{4\pi} p_\lambda(\Omega,\Omega') I_\lambda(\vec{x}',\vec{\Omega}') d\Omega' \tag{17}$$

$$\mathrm{P}_{L_{sca},\lambda} = k_{sca,\lambda} e^{-k_{sca,\lambda} l_{sca}(\vec{x}')} \tag{18}$$

$$W_i = \Phi_{0,\lambda} \prod_{k=0}^{n_i} q_{k+1} e^{-k_{ext,\lambda} l_{k+1}} \tag{19}$$

where $\Phi_{t,\lambda,MC} = T_{\lambda,MC}$ is the Monte-Carlo estimate of the transmittivity, N is the number of Monte-Carlo realizations and W_i is the Monte-Carlo weight computed following each ray from the source until it leaves the domain (details on the computation algorithm is given in Appendix A). As drawn on Fig.8, the first direction of the ray $\vec{\Omega}_0$ is normal and incident to the PMMA plate. A Bernoulli trial is drawn at each interface intersection to define whether the ray is reflected ($\rho_{\lambda,i\to t}$) or refracted ($1-\rho_{\lambda,i\to t}$). If it is refracted on the two first interfaces, the ray enters the colloidal medium which effective radiative properties have been previously defined (section 2.3). The ray will then suffer scattering and absorption events in the TiO_2 particles suspension. Thus, the radiative intensity in the colloidal medium is obtained by Eq.17 which considers scattering events sampling. The first sampling on the right-hand-side of Eq.17 is the scattering length l_{sca} which is defined using the probability density function $\mathrm{P}_{L_{sca},\lambda}$ (Eq.18). The second sampling is the scattering direction $\vec{\Omega}_{k+1}$ which is defined using the angle-dependent scattering function $p_\lambda(\vec{\Omega},\vec{\Omega}')$ calculated in section 2.3. Absorption event along the ray path is included in the Monte-Carlo weight expression (Eq.19) making the product of the transmission by absorption along the ray path. The absorption is

considered through $k_{abs,\lambda}$ of TiO_2 calculated (Eq.5) using the previously defined $E_{abs,\lambda}$. This expression also includes the source directional flux and the number of direction changes (by scattering, refraction or reflection) n_i along the path. Note that q_{k+1} ensures the probability of pursuing the random walk. This probability is unity except when the ray leaves the PMMA cell on the source side or when TIR occurs in PMMA, in which cases this probability is zero and the random walk is stopped (resulting in $W_i = 0$). The estimation of the transmittivity is reached through the calculation of the mean of Monte-Carlo transmitted flux after N realizations of the random walks.

The local available radiant energy $G_{\vec{x},\lambda}$ (Eq. 20) is estimated by another Monte-Carlo algorithm ($G_{\vec{x},\lambda,MC}$) :

$$G_{\vec{x},\lambda} = \int_{4\pi} I_\lambda(\vec{x},\vec{\Omega}) d\Omega \tag{20}$$

This additional algorithm includes a reverse formulation of the bundle of rays paths and a radiative intensity splitting between the direct and scattered components (the algorithm is presented in Appendix B).

3.2. Two-flux approximation

The general RTE (Eq. 9) can be simplified because of the azimuthal independence described in section 2.3., which allows to simplify the equation from the ϕ angle [44]:

$$\cos\theta \frac{dI_\lambda(x,\theta)}{dx} = -(k_{abs,\lambda} + k_{sca,\lambda}) I_\lambda(x,\theta) + \frac{k_{sca,\lambda}}{2} \int_0^\pi I_\lambda(x,\theta') p_\lambda(\theta,\theta') \sin\theta' d\theta' \tag{21}$$

Here the observation direction $\vec{u}$ was set on the x-axis. For a given angular dependence of the intensities and averaging Eq. (21) on both backward and forward hemispheres over all directions leads to a two-equations system in which the radiant energy flux going forward, called Φ_λ^+ and the radiant energy flux going backward, called Φ_λ^- are separated. These equations must be written considering the irradiation conditions and the light propagation inside the studied system. Here the irradiation is provided by a collimated source and the light propagation inside the medium is considered collimated in both forward and backward directions because the phase function of TiO_2 particles on Figure 6.B. is strongly forward oriented in the observation direction ($\theta \approx 0°$). Thus, the equation system is [45]:

$$\begin{cases} \dfrac{d\Phi_\lambda^+}{dx} = -a_{\lambda,c}\Phi_\lambda^+ + \sigma_{\lambda,c}(\Phi_\lambda^- - \Phi_\lambda^+) \\ \dfrac{d\Phi_\lambda^-}{dx} = a_{\lambda,c}\Phi_\lambda^- + \sigma_{\lambda,c}(\Phi_\lambda^- - \Phi_\lambda^+) \end{cases} \tag{22}$$

where $a_{\lambda,c}$ and $\sigma_{\lambda,c}$ are respectively the two-flux "collimated" coefficients of absorption and diffusion defined as follows :

$$a_{\lambda,c} = \frac{k_{abs,\lambda}}{\cos\theta} \qquad \text{and} \qquad \sigma_{\lambda,c} = \frac{bk_{sca,\lambda}}{\cos\theta} \tag{23}$$

where b represents the backscattered radiative fraction, which can be calculated from the angle-dependent scattering phase function. Note that the collimated irradiation and the observation have the same direction, thus, $\cos\theta$ value is 1 in our conditions.

This system of differential equations can be integrated, by setting the appropriate boundary conditions. Here the measuring cell is irradiated on one side (x=0) with a collimated source which radiant energy flux $\Phi_{0,\lambda}$ is normalized to 1. The opposite side of the cell is not irradiated, and no reflection occurs at the exit of the medium. It should also be indicated that

the cell interfaces effect (air/PMMA and medium/PMMA) on light refraction and extinction are at first neglected within this approach. Thus, the following boundary conditions were set:

$$x = 0 \qquad \Phi_\lambda^+ = 1 \tag{24}$$

$$x = L \qquad \Phi_\lambda^- = 0 \tag{25}$$

The integration of the differential equation system (22) using (24) and (25) boundary conditions gives:

$$\Phi_\lambda^+(x) = \frac{(1+\alpha_{\lambda,c})^2 e^{\delta_{\lambda,c}(L-x)} + (1-\alpha_{\lambda,c})^2 e^{\delta_{\lambda,c}(x-L)}}{(1+\alpha_{\lambda,c})^2 e^{\delta_{\lambda,c}L} - (1-\alpha_{\lambda,c})^2 e^{-\delta_{\lambda,c}L}} \tag{26}$$

$$\Phi_\lambda^-(x) = \frac{(1-\alpha_{\lambda,c}^2)(e^{\delta_{\lambda,c}(L-x)} - e^{\delta_{\lambda,c}(x-L)})}{(1+\alpha_{\lambda,c})^2 e^{\delta_{\lambda,c}L} - (1-\alpha_{\lambda,c})^2 e^{-\delta_{\lambda,c}L}} \tag{27}$$

where $\alpha_{\lambda,c}$ and $\delta_{\lambda,c}$ are defined as follows:

$$\alpha_{\lambda,c} = \sqrt{\frac{E_{abs,\lambda}}{E_{abs,\lambda} + 2bE_{sca,\lambda}}} \tag{28}$$

$$\delta_{\lambda,c} = C_{susp}\sqrt{E_{abs,\lambda}(E_{abs,\lambda} + 2bE_{sca,\lambda})} \tag{29}$$

The two-flux (TF) radiant energy flux $q_{x,\lambda,TF}$ and the radiant energy available $G_{x,\lambda,TF}$ can then be calculated from the forward and backward fluxes so that:

$$q_{x,\lambda,TF} = \Phi_{\lambda,c}^+ - \Phi_{\lambda,c}^- = 2\alpha_{\lambda,c}\frac{(1-\alpha_{\lambda,c})e^{\delta_{\lambda,c}(x-L)} + (1+\alpha_{\lambda,c})e^{-\delta_{\lambda,c}(x-L)}}{(1+\alpha_{\lambda,c})^2 e^{\delta_{\lambda,c}L} - (1-\alpha_{\lambda,c})^2 e^{-\delta_{\lambda,c}L}} \tag{30}$$

$$G_{x,\lambda,TF} = \Phi^{+}_{\lambda,c} + \Phi^{-}_{\lambda,c} = 2\frac{(1-\alpha_{\lambda,c})e^{\delta_{\lambda,c}(x-L)} + (1+\alpha_{\lambda,c})e^{-\delta_{\lambda,c}(x-L)}}{(1+\alpha_{\lambda,c})^2 e^{\delta_{\lambda,c}L} - (1-\alpha_{\lambda,c})^2 e^{-\delta_{\lambda,c}L}} \tag{31}$$

The expression of the transmittance at the exit of the measuring cell can be obtained by calculating the radiant energy flux $q_{x,\lambda}$ at x=L:

$$T_{\lambda,TF} = q_{L,\lambda,TF} = \frac{4\alpha_{\lambda,c}}{(1+\alpha_{\lambda,c})^2 e^{\delta_{\lambda,c}L} - (1-\alpha_{\lambda,c})^2 e^{-\delta_{\lambda,c}L}} \tag{32}$$

However, it can easily be noticed that these functions exhibit undefined limits when the specific absorption coefficient $E_{abs,\lambda}$ of the studied suspension tend to be null. Thus, this limit was easily overcome by re-integrating the differential equations system (Eq. (22)) setting $a_{\lambda,c} = 0$ in the equations. When the specific absorption coefficient is null, the definition of radiant energy flux (Eq.(30), the radiant available energy (Eq.(31)), and the transmittance (Eq.(11)) are defined as:

$$q_{x,\lambda,TF} = T_{\lambda,TF} = \frac{1}{\sigma_{\lambda,c}L + 1} \tag{33}$$

$$G_{x,\lambda,TF} = \frac{2\sigma_{\lambda,c}(L-x)+1}{\sigma_{\lambda,c}L + 1} \tag{34}$$

Note that the wavelength and energy modifications induced by the refractive index difference outside and inside the medium were considered using Eq. (14) to correct $G_{x,\lambda,TF}$. This analytical approach was applied to the study of TiO_2 suspensions using the radiative properties calculated from Mie's theory, in order to model both transmitted radiant energy and the local available energy within the suspended medium.

Corrections can be provided to the two-flux approach to consider the interfaces surrounding the media. The PMMA cell entrance interfaces can be taken into account by applying a correction factor to $T_{\lambda,TF}$ and $G_{x,\lambda,TF}$ which corresponds to Fresnel's reflection at Air/PMMA and PMMA/Water interfaces. Moreover, total internal reflections in the exit PMMA plate, occurring when photons exit the media with an angle, superior to a defined value, can be considered for $T_{\lambda,TF}$ correction. Snell's law leads to define the value of the Brewster angle which is 48.75°. The ratio of photons inducing TIR in PMMA was assessed from the calculation of: (i) the mean length of diffusion occurring in the media and (ii) the deviation from normal direction induced by each diffusion.

Wavelength	**350 nm**		**390 nm**		**410 nm**		**450 nm**		**500 nm**	
Concentration	$\mathbf{n_{diff}}$	$\mathbf{r_{TIR}}$	$\mathbf{n_{diff}}$	$\mathbf{r_{TIR}}$	$\mathbf{n_{diff}}$	$\mathbf{r_{TIR}}$	$\mathbf{n_{diff}}$	$\mathbf{r_{TIR}}$	$\mathbf{n_{diff}}$	$\mathbf{r_{TIR}}$
0.01 kg.m^{-3}	0	0	0	0	0	0	0	0	0	0
1 kg.m^{-3}	0.8	0	0.9	0	1.4	0.22	1.4	0.21	1.4	0.2
3 kg.m^{-3}	2.4	0	2.5	0	4.3	0.46	4.3	0.45	4.1	0.44

Table 2. *Number of diffusions n_{diff} and TIR ratio r_{TIR} calculated at different concentrations (0.01; 1 and 3 kg.m^{-3}) and wavelength (350; 390; 410; 450 and 500 nm).*

The mean length of diffusion was calculated from the probability density function $P_{L_{sca},\lambda}$ by calculating the mean of the probability function. As the TiO_2 scattering is forward, the number of scattering was approximated by dividing the medium length, i.e. 0.02 m by the mean diffusion length. This approach led to the determination of the mean number of diffusions for different considered wavelength and concentration, reported in table 2. The deviation angle from normal direction induced by one diffusion was then obtained from the angle-dependent scattering function, by representing the cumulative distribution of the phase

function relative to the deviation angle from normal direction. Finally, the photon ratio exceeding a deviation from the normal direction of 48.75° and inducing TIR in PMMA was assessed from $P_{\perp,\lambda}(\theta,\theta')$ function, corresponding to the cumulative distribution of the phase function represented as a function of the total deviation angle from the normal axis after n diffusions. The total deviation angle is then the deviation angle induced by one diffusion multiplied by the total number of diffusions n_{diff}. The total TIR ratio r_{TIR}, which will be withdrawn to the TF model, was reported in table 2. The two-flux model corrected by the interface effect will be later mentioned as TF_C.

3.3 Model validation

The transmittance given by the TF, TF_C and MC models were compared to the experimental measures to validate and discuss the accuracy of these models and particularly the interfaces management through each of them. The transmittance obtained for three TiO_2 suspension concentrations were represented in Figure 9 to cover the whole concentration scale.

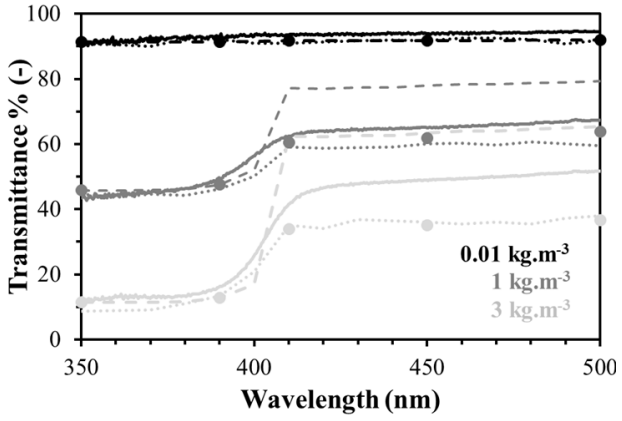


Figure 9. *Comparison of MC (dotted lines), TF (dashed lines) and TF_c (●) for the transmittance representation of TiO_2 for three concentrations: 0.01; 1 and 3 kg.m^{-3}. Comparison with the experimentally measured transmittance (continuous lines).*

First, one may observe that all model curves fit well with the corresponding experimental curves in the UV region for all TiO_2 suspension concentrations, where absorption occurs in the medium. Regarding the visible region, where only scattering occurs, all models fit well for low diffusive media, i.e. 0.01 $kg.m^{-3}$ TiO_2 concentration. However, one can observe that increasing TiO_2 concentration up to 1 $kg.m^{-3}$ leads to a misfit of about 30% of the TF model with the experimental curve, while TF_C and MC simulated transmittance whom curves match well each other and are less than 10% below the experimental one. For high diffusive media, corresponding to the 3 $kg.m^{-3}$ TiO_2 concentration, all models mismatch the experimental curves. Indeed, TF transmittance is 40 % higher than the experimental curve, and TF_C and MC simulations are 20% lower.

Following these observations, the first interesting point which emerges is the agreement between TF_C and MC models, which led us to assert that the empirical correction applied to TF model was quite good to consider the medium surrounding interfacial effects. As expected from Mie theory, it can be asserted that the radiative properties are probably well defined in the interest wavelength of TiO_2 use, i.e. near UV region, where the models match the experimental curves whatever the suspension concentration. The MC and TF_C models were found to match each other at high concentrations but are both mismatching the experimental curve. This observation highlights a limit of our experimental set-up, whose configuration is not well adapted for the transmittance assessment of highly diffusive media.

4. Local volumetric rate of radiant energy absorbed

The transmittance assessment from models allowed to highlight their consistency, but the real interest in their use remain in the radiant energy field description inside the system. The knowledge of the local radiant energy is of great importance for the formulation of photoreactions kinetic laws. In the present case study, note that the use of TiO_2 catalyst in

photoreactors requires near UV photons to induce electron excitation. This excitation corresponds to the absorption range of TiO_2 particles in UV region. Thus, the interest wavelength range of local radiant energy assessment is around 370 nm. TF and MC models allowed to represent the 1D local available radiant energy by plotting $G_{x,370\,nm,TF}$ and $G_{\vec{x},370\,nm,MC}$ relative to the thickness of the medium travelled x/L, for suspensions concentration from 0.01 to 3 kg.m^{-3} (Figure 10.A).

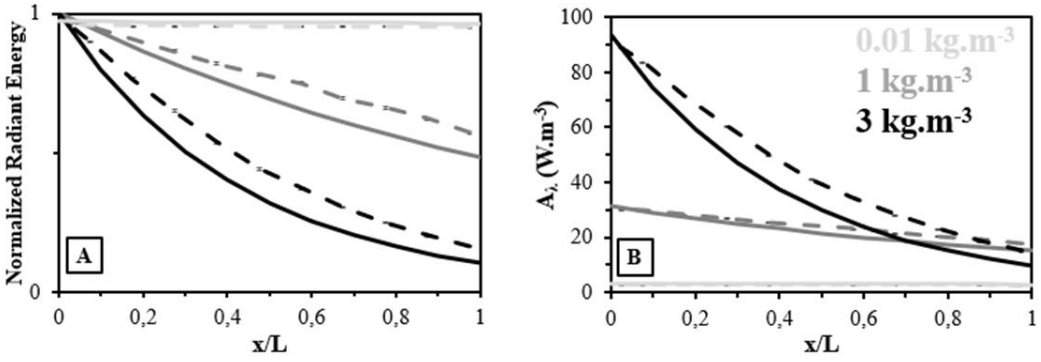


Figure 10. *Representation of the radiant energy within the TiO_2 suspension in the PMMA cell by MC (dashed lines) and TF (continuous lines) models, as a function of the location in the medium : normalized available radiant energy (A) and Local Volumetric Rate of Radiant Energy Absorbed LVREA (B). The wavelength is 370 nm.*

Both models exhibit similar radiant energy profile whatever the suspension concentration, which indicates that the two approximated and rigorous approaches are adapted to model the radiative transfer of such colloidal media, composed by highly absorptive particles with forward phase function. Note that the profile varies drastically with the change in suspension concentration, showing the importance of catalyst concentration in photocatalytic processes using particulate media. We were then able to estimate the most relevant local volumetric rate of radiant energy absorbed $A_\lambda(x)$ in W.m^{-3}(Figure 10.B) with Eq.(35):

$$A_\lambda(x) = k_{abs,\lambda}.G(x) \tag{35}$$

As expected, the absorbed radiant energy profile is almost null along the medium for suspension concentration as low as 0.01 $kg.m^{-3}$. Then it can be observed that increasing concentration lead to the augmentation of the locally absorbed radiant energy and to an evolution of the local absorption profile from a linear change along the medium (1 $kg.m^{-3}$) to an exponential decline-like profile (3 $kg.m^{-3}$).

It should be kept in mind that the immediate goal of this work was not to provide quantitative values of our particular system, but rather to develop a rigorous method composed of both experimental and theoretical approaches for the accurate radiative analysis of widely used parallel-plate photoreactors using particulate media.

To go further in the analysis of particulate media, future studies will include the investigation of the quantum yield of a reaction, such as $OH^{\bullet}$ and $O_2^{-\bullet}$ radicals generation for example in the case of TiO_2 photocatalytic reactions. Moreover, complex particulate media such as doped or composite particles will also be investigated.

5. Conclusion

In this article, an experimental and theoretical coupled approach, allowing the description of radiative transfer in particulate media was presented. This approach meets the need of local radiant energy description in systems where photoreactions/photobioreactions are not linearly dependent to the incident radiant energy, which correspond to a lot of real reactions.

First, the morphological characteristics of the Aeroperl® P25/20 TiO_2 case study material were presented. It was noted that this material is composed of two TiO_2 crystalline phases and the powder particles are heterogeneous in size. Thus, it was needed to define an effective refractive index of the material to allow the study of its radiative properties.

On the second part, an experimental optical bench was set up to identify experimentally by inversion in simple scattering conditions the absorption specific coefficient of the case study powder material. On the other side, Mie theory and the well-known BHMIE program were used to compute the particle radiative properties and the Bruggeman formula to obtain the heterogeneous radiative properties for the polydispersion of TiO_2. The correlation between experimental and theoretical approaches was consistent and led to the obtention of the material radiative properties.

A third part consisted in two different resolutions of the radiative transfer equation to describe the local radiant energy in parallel-plate reactor: (i) the Monte Carlo rigorous method and (ii) an approximate Two-Flux approach. First, the previously made transmittance measurements using the optical bench were modeled through these two methods. This step allowed to assess the consistency between experimental transmittance values and the simulated ones, which was found to be acceptable for low and medium TiO_2 powder concentration (0.01 to 1 $kg.m^{-3}$). However, it was noticed that both models, although similar for low and medium concentration transmittance description, failed in representing transmittance for highly concentrated particulate media (3 $kg.m^{-3}$) , where a lot of scattering events occur. The models were finally both used to describe the LVREA, which would be for great interest for future studies about the TiO_2 photocatalytic kinetic reactions in simple geometry reactors.

Acknowledgements

This work has been supported by the Occitanie Region in France, by European Regional Development Fund (ERDF) provided by the European Union and by a research and society fund from the project Photodepoll n°19015248. This work was also sponsored by a public grant overseen by the French National Agency as part of the "Investissements d'Avenir" through the IMobS3 Laboratory of Excellence (ANR-10-LABX-0016) and the IDEX-ISITE initiative CAP 20-25 (ANR-16-IDEX-0001).

References

[1] Degrenne B, Pruvost J, Christophe G, Cornet JF, Cogne G, Legrand J. Investigation of the combined effects of acetate and photobioreactor illuminated fraction in the induction of anoxia for hydrogen production by Chlamydomonasreinhardti. International Journal of Hydrogen Energy. 2010; 35(19): 10741-10749.

[2] Pankratz S, Kumar M, Oyedun AO, Gemechu E, Kumar A. Environmental performances of diluents and hydrogen production pathways from microalgae in cold climates: Open raceway ponds and photobioreactors coupled with thermochemical conversion. Algal Research. 2020; 47:101815.

[3] Adessi A, De Philippis R. Photobioreactor design and illumination systems for H_2production with anoxygenic photosynthetic bacteria: A review. International Journal of Hydrogen Energy. 2014; 39 (7): 3127-3141.

[4] Castellanos RM, Bassin JP, Dezotti M, Boaventura RAR, Vilar VJP. Tub-in-tube membrane reactor for heterogeneous TiO_2photocatalysis with radial addition of H_2O_2. Chemical Engineering Journal. 2020; 395: 124998.

[5] Spasiano D, Marotta R, Malato S, Fernandez-Ibañez P, Di Somma I. Solar photocatalysis: materials, reactors, some commercial, and pre-industrialized applications. A comprehensive approach. Applied Catalysis B: Environmental. 2015; 170-171: 90-123.

[6] Plantard G, Goetz V. Kinetic and efficiency of TiO_2-coated on foam or tissue and TiO_2-suspension in a photocatalytic reactor applied to the degradation of the 2,4-dichlorophenol. Journal of Photochemistry and Photobiology A: Chemistry. 2011; 222 (1): 111-116.

[7] Leeds AR. Action of light on the soluble iodides, with the outlines of a new method in actinometry. Journal of American Chemical Society. 1880; 2: 249-270.

[8] Laqua K, Schrader B, Hoffmann GG, Moore DS, Vo-Dinh T. Detection of radiation. SpectrochimicaActa Part B: Atomic Spectroscopy. 1997; 52 (5): 537-552.

[9] Abraham F, Arab-Chapelet B, Rivenet M, Tamain C, Grandjean S. Actinide oxalates, solid state structures and applications. Coordination Chemistry Reviews. 2014; 266-267: 28-68.

[10] Hatchard CG, Parker CA. A new sensitive chemical actinometer. II. Potassium ferrioxalate as a standard chemical actinometer. Proceedings of the Royal Society A. 1956; 235: 518-536.

[11] Behnajady MA, Modirshahla N, Shokri M, Vahid B. Design equation with mathematical kinetic modeling for photooxidative degradation of C.I. Acid Orange 7 in an annular continuous-flow photoreactor. Journal of Hazardous Materials. 2008; 165 (1-3): 168-173.

[12] Elkanzi EM, Khleng GB. H_2O_2/UV degradation kinetics of isoprene in aqueous solution. Journal of Hazardous Materials. 2000; B73: 55-62.

[13] Bitaubé Pérez E, Caro Pina I, Pérez Rodriguez L. Kinetic model for growth of Phaeodactylumtricornutum in intensive culture photobioreactor. Biochemical Engineering Journal. 2008; 40 (3): 520-525.

[14] Bagwasi S, Tian B, Zhang J, Nasir M. Synthesis, characterization and application of bismuth and co-doped TiO_2: a visible light active photocatalyst. Chemical Engineering Journal. 2013; 217: 108-118.

[15] Al-Mamun MR, Kader S, Islam MS, Khan MZH. Photocatalytic activity improvement and application of UV-TiO_2photocatalysis in textile wastewater treatment: A review. Journal of Environmental Chemical Engineering. 2019; 7 (5): 103248.

[16] Janin T, Goetz V, Brosillon S, Plantard G. Solar photocatalytic mineralization of 2,4-dichlorophenol and mixtures of pesticides: Kinetic model of mineralization. Solar Energy. 2013; 87: 127-135.

[17] Huang SM, Weng CH, Tzeng JH, Huang YZ, Anotai J, Yen LT, Chang CJ, Lin YT. Kinetic study and performance comparison of TiO_2-mediated visible-light-responsive photocatalysts for the inactivation of Aspergillus Niger. Science of the Total Environment. 2019; 692: 975-983.

[18] Khalilzadeh A, Shariati A. Photoreduction of CO_2 over heterogeneous modified TiO_2 nanoparticles under visible light irradiation: Synthesis, process, and kinetic study. Solar Energy. 2018; 164: 251-261.

[19] Geng QJ, Wang XK, Tang SF. Heterogeneous Photocatalytic Degradation Kinetic of Gaseous Ammonia Over Nano-TiO_2 Supported on Latex Paint Film. Biomedical and Environmental Sciences. 2008; 21 (2): 118-123.

[20] Sabate J, Anderson MA, Kikkawa H, Edwards M, Hill CG. A kinetic study of the photocatalytic degradation of 3-Chlorosalicylic Acid over TiO_2 membranes supported on glass. Journal of catalysis. 1991; 127: 167-177.

[21] Plantard G, Goetz V. Correlations between optical, specific surface and photocatalytic properties of media integrated in a photo-reactor. Chemical Engineering Journal. 2014; 252: 194-201.

[22] DeVore JR. Refractive indices of Rutile and Sphalerite. Journal of the Optical Society of America. 1951; 41 (6): 416-419.

[23] Kischkat J, Peters S, Gruska B, Semtsiv M, Chashnikova M, Klinkmüller M, Fedosenko O, Machulik S, Aleksandrova A, Monastyrskyi G, Flores Y, Masselink WT. Mid-infrared optical properties of thin films of aluminum oxide, titanium dioxide, silicon dioxide, aluminum nitride, and silicon nitride. Applied Optics. 2012; 51: 6789-6798.

[24] Bodurov I, Vlaeva I, Viraneva A, Yovcheva T, Sainov S. Modified design of a laser refractometer. Nanoscience& Nanotechnology. 2016; 16: 31-33.

[25] Auvinen S, Alatalo M, Haario H, Vartiainen E, Jalava JP, Lamminmäki RJ. Refractive index functions of TiO_2 nanoparticles. Journal of Physical Chemistry C. 2013; 117 (7): 3503-3512.

[26] Siefke T, Kroker S, Pfeiffer K, Puffky O, Dietrich K, Franta D, Ohlidal I, Szeghalmi A, Kley EB, Tünnermann A. Materials pushing the application limits of wire grid polarizers further into the deep ultraviolet spectral range. Advanced Optical Materials. 2016; 4: 1780-1786.

[27] Sarkar S, Gupta V, Kumar M, Schubert J, Probst PT, Joseph J, König TAF. Hybridized guided-mode resonances via colloidal plasmonic self-assembled grating. ACS Applied Materials Interfaces. 2019; 11: 13752-13760.

[28] Jalava JP, Taavitsainen VM, Lamminkmäki RJ, Lindholm M, Auvinen S, Alatalo M, Vartiainen E, Haario H. Modeling TiO_2's refractive index function from bulk to nanoparticles. Journal of Quantitative Spectroscopy & Radiative Transfer. 2015; 167: 105-118.

[29] Bruggeman DAG. Berechnung verschiedener physikalischer Konstanten von heterogenen substanzen. Annal of Physics. 1935; 24: 636-679.

[30] Markel V. Introduction to the Maxwell Garnett approximation: tutorial. Journal of the Optical Society Of America A. 2016; 33 (7): 1244-1256.

[31] Lorenz LV. Vidensk Selk Skr. 1890; 6: 1-62.

[32] Mie G. Beitragezur Optik truber Medien, speziell kolloidaler metallosungen. Annalen der physik. 1908; 25: 377-445.

[33] Bohren CF, Huffman DR. Absorption and Scattering of Light by Small Particles. John Wiley and Sons, New York. 1983.

[34] Modest MF. Radiative properties of particulate media. Radiative Heat Transfer. 2003; 361-412. doi: 10.1016/B978-012503163-9/50012-6.

[35] Li X, Xie L, Zheng X. The comparison between the Mie theory and the Rayleigh approximation to calculate the EM scattering by partially charged sand. Journal of Quantitative Spectroscopy and Radiative Transfer. 2012; 113 (3): 251-258.

[36] Gouesbet G. Gradient, scattering and other kinds of longitudinal optical forces exerted by off-axis Bessel beams in the Rayleigh regime in the framework of generalized Lorenz-Mie theory. Journal of Quantitative Spectroscopy and Radiative Transfer. 2020; 246: 106913.

[37] Beach HL, Özisik MN, Siewert CE. Radiative transfer in linearly anisotropic-scattering, conservative and non-conservative slabs with reflective boundaries. International Journal of Heat and Mass Transfer. 1971; 14 (10): 1551-1565.

[38] Pilon L, Berberoglu H, Kandilian R. Radiation transfer in photobiological carbon dioxide fixation and fuel production by microalgae. Journal of Quantitative Spectroscopy& Radiative Transfer. 2011; 112: 2639-2660.

[39] Davies-Colley RJ, Pridmore RD, Hewitt JE. Optical properties and reflectance spectra of 3 shallow lakes obtained from a spectrophotometric study. NZ Journal of Marine and Freshwater Research. 1983; 17: 445-459.

[40] Delatorre J, Baud G, Bézian JJ, Blanco S, Caliot C, Cornet JF, Coustet C, Dauchet J, El Hafi M, Eymet V, Fournier R, Gautrais J, Gourmel O, Joseph D, Meilhac N, Pajot A, Paulin M, Perez P, Piaud B, Roger M, Rolland J, Veynandt F, Weitz S. Monte Carlo advances and concentrated solar applications. Solar Energy. 2014; 103: 653-681.

[41] Dauchet J, Cornet JF, Gros F, Roudet M, Dussap CG. Photobioreactor modeling and radiative transfer analysis for engineering purposes. Advances in Chemical Engineering. 2016; 48: 1-106.

[42] Veach E. Robust Monte Carlo Methods for Light Transport Simulation. PhD dissertation, Stanford University. 1997.

[43] Pauly M, Kollig T, Keller A. Metropolis light transport for participating media. B. Peroche & H. Rushmeier (Eds), Rendering Techniques 20000, Springer Vienna. 2000; 11-22.

[44] Chandrasekhar S. Radiative Transfer. Dover, New York. 1960.

[45] Hottel HC, Sarofim AF. Radiative transfer. Mc Graw-Hill Book Company. 1967.

Appendix

Click here to download Supplementary Material: appendix.pdf

***Declaration of Interest Statement**

Declaration of interests

☒ The authors declare that they have no known competing financial interests or personal relationships that could have appeared to influence the work reported in this paper.

☐The authors declare the following financial interests/personal relationships which may be considered as potential competing interests: